Applied Surface Science 695 (2025) 162923

Contents lists available at ScienceDirect

Applied Surface Science

journal homepage: www.elsevier.com/locate/apsusc

Full Length Article

Variations of electronic properties on the behavior of visible light-triggered TiO_2 + Au photocatalysts

Špela Slapničar [a], Gregor Žerjav [a], Matevž Roškarič [a], Janez Zavašnik [b], Albin Pintar [a,*]

[a] Department of Inorganic Chemistry and Technology, National Institute of Chemistry, Hajdrihova 19, SI-1001 Ljubljana, Slovenia
[b] Gaseous Electronics, Jožef Stefan Institute, Jamova 39, SI-1000 Ljubljana, Slovenia

ARTICLE INFO

Keywords:
Titanium dioxide
Gold nanoparticles
Wet impregnation
Heterogeneous photocatalysis
Localized surface plasmon resonance effect

ABSTRACT

In this study, we investigated the influence of TiO_2 supports on the structural and catalytic properties of TiO_2 + Au catalysts (1 wt% Au) using anatase TiO_2 nanorods (TNR, S_{BET} = 106 m^2/g) or nanospheres (TNP, S_{BET} = 86 m^2/g). The majority of Au particles in the prepared TiO_2 + Au catalysts were in the range of 20–30 nm, with slight differences observed between the TNR + Au and TNP + Au samples. It is noteworthy that the addition of Au did not significantly change the specific surface area and crystallinity of the TiO_2 supports. Evaluation of photocatalytic activity using $ABTS^{\bullet+}$ cation oxidation, DMPO/DMSO spin trapping and bisphenol A (BPA) degradation under visible-light illumination showed different behaviour of TNR + Au and TNP + Au catalysts. The TNR + Au catalyst produced mainly e^-, while the TNP + Au catalyst exhibited efficient $O_2^{\bullet-}$ production, which was confirmed by electron paramagnetic resonance spin trapping analyses. Conversely, due to its high Schottky barrier height (SBH) and the properties of the Au nanoparticles, the TNR + Au catalyst could not facilitate an oxygen reduction reaction but effectively produced e^- as it reduced $ABTS^{\bullet+}$. The results show that the degradation of BPA in the presence of the TNR + Au photocatalyst occurs through the involvement of e^- and a small amount of hydroxyl radicals ($OH^{\bullet}$). Comprehensive characterization techniques provided insights into the intricate relationships between catalyst structure, composition and catalytic activity.

1. Introduction

Heterogeneous photocatalysis, which utilizes the synergistic properties of the semiconductor titanium dioxide (TiO_2), has proven to be a highly effective advanced oxidation process (AOP) for wastewater treatment. TiO_2 is one of the most commonly used semiconducting oxides for the removal of hazardous pollutants from wastewater. The TiO_2 catalyst has many advantageous properties, e.g. low cost, low toxicity, high stability, availability and high photocatalytic activity [1]. However, its main disadvantage lies in its wide band gap (3.0–3.4 eV) and the fast recombination rate of the charge carriers. The width of the band gap depends on the morphology of TiO_2. It is known that TiO_2 occurs in nature in three polymorphic forms: rutile, brookite and anatase [2]. Rutile is stable at higher temperatures, brookite usually occurs in minerals with an orthorhombic crystal structure and anatase is stable at low temperatures. In this study, anatase TiO_2 was used, which is known to be the most active form [3]. TiO_2, a well-established photocatalyst, exhibits various morphologies, including nanospheres, nanorods, nanowires, and nanotubes [4–6]. The applications of anatase are difficult because the quantum power is low and UV light is required to trigger its catalytic activity [7]. The wide band gap restricts the catalytic activation of TiO_2 to UV light and so it can utilize only 5 % of the solar spectrum. The strategic deposition of plasmonic metal nanoparticles (e.g. Au nanoparticles (NPs)) on anatase TiO_2 surfaces is promising to harness visible light and near-infrared radiation from the solar spectrum. In particular, the integration of TiO_2 with gold (Au) in the form of TiO_2 + Au catalysts has shown remarkable potential for the utilization of visible light for efficient pollutant degradation. Au NPs have been widely used in nanotechnology, because of their stability, biocompatibility, non-toxicity, robustness and minimal oxidation tendency [8].

A Schottky barrier (SB) is formed at the interface between the metal (Au) and the semiconductor (TiO_2). The Schottky barrier height (SBH) is very important, as it influences the mobility of the plasmon-induced "hot electrons" at the Au/TiO_2 interface and consequently the catalytic efficiency [9,10]. Moon et al. [11] found that the activity of the Au/TiO_2 material for catalytic reactions is better when the SBH value is lower. A study by Wang et al. [12] shows that decreasing the SBH not only improves the transfer of conduction band (CB) electrons (e^-) from

* Corresponding author.
E-mail address: albin.pintar@ki.si (A. Pintar).

https://doi.org/10.1016/j.apsusc.2025.162923
Received 14 August 2024; Received in revised form 14 February 2025; Accepted 7 March 2025
Available online 8 March 2025

TiO_2 to Au upon UV excitation of TiO_2 but also facilitates the migration of hot e^- from plasmonic Au to TiO_2 upon visible-light irradiation. Žerjav et al. [13] confirmed in their article that the Au/TiO_2 sample with the lowest SBH was the most effective in combating pollutants, while the study of Slapničar et al. [14] points to completely different conclusions, although the basic chemistry is the same. This requires further in-depth studies to explain the differences in the behaviour of the photocatalysts in question.

The photocatalytic activity of TiO_2 + Au materials is strongly influenced by various factors (e.g. form of TiO_2 and Au, synthesis method, Au loading and Au size). Each form imparts different optical and electronic properties to TiO_2 + Au, which affect its performance in photocatalytic processes. TiO_2 + Au catalysts are used for various applications, including the degradation of pollutants in water. One of the well-known and globally prevalent contaminants is bisphenol A (BPA), which is an endocrine disruptor commonly found in plastic food and beverage packaging. BPA is an antioxidant that is non-biodegradable and highly resistant to chemical degradation, posing a risk to human and animal health [15]. Several studies have shown that TiO_2 + Au catalysts successfully remove BPA from water when used in the AOP [16]. Two types of primary oxidation mechanisms are known. In indirect oxidation, hydroxyl radicals ($OH^\bullet$) is formed following the reaction between a water molecule adsorbed on the catalyst surface and h^+, followed by the reaction of $OH^\bullet$ with an organic molecule such as BPA. In contrast, direct oxidation takes place at the surface of the semiconductor, where adsorbed organic molecules react with a valence band (VB) hole (h^+) [17].

The overall aim of this study is to systematically explore and elucidate the influence of the TiO_2 + Au synthesis and the effect of TiO_2 and Au shapes and sizes on the optical, electronic and photocatalytic properties of TiO_2 + Au catalysts in the context of wastewater treatment. We present a thorough investigation of TiO_2 + Au catalysts, varying the TiO_2 shapes and keeping the Au loading at 1.0 wt%. We focus on Au in this study because it is an ideal plasmonic partner for TiO_2 in wastewater treatment due to its advantageous properties such as biocompatibility, non-toxicity, robustness and minimal oxidation tendency. Due to the different correlations between SBH value and catalyst activity (in the aforementioned studies [11–14]), we decided to investigate in detail the processes that influence catalyst activity. With this study, we aim to make a valuable contribution to the development and optimization of TiO_2 + Au catalysts for wastewater treatment and pave the way for improved efficiency and selectivity in pollutant degradation. The results of this study are of great significance to the broader field of plasmonic photocatalysis as they provide a nuanced understanding of the role of TiO_2 morphology in shaping the performance of TiO_2 + Au catalysts under visible-light irradiation.

2. Experimental

2.1. Materials

TiO_2 precursor DT-51 was provided by the company CristalACTiV™. Sodium hydroxide (NaOH, ≥98 %, Merck), hydrochloric acid (HCl, fuming 37 %, ≤1 ppm free chlorine, Merck), gold (III) chloride hydrate ($HAuCl_4 \cdot xH_2O$, ~50 % Au basis, Sigma Aldrich), absolute ethanol (C_2H_5OH, ≥99.5 %, Carlo Erba reagents), coumarin (COUM, ≥98 %, Thermo Fisher), 2,2′-azino-bis-(3-ethylbenzothiazoline-6-sulfonic acid) cation ($ABTS^{\bullet+}$, ≥98 %, Sigma Aldrich), potassium persulfate ($K_2S_2O_8$, ≥99 %, Sigma Aldrich), 5–5-dimethyl-1-pyrroline-N-oxide (DMPO, ≥98.0 %, Sigma Aldrich) dissolved in dimethyl sulfoxide (DMSO, ≥99.9 %, Sigma Aldrich), 2,2,6,6-tetramethylpiperidine (TEMP, ≥99 %, Sigma Aldrich) and bisphenol A (BPA, ≥99 %, Sigma Aldrich) were used as received. All aqueous solutions used in this work were prepared with ultrapure water (18.2 MΩ cm) and stored in the dark at 4 °C.

2.2. Catalyst synthesis

In this research, we used titanate nanospheres (TNP) and titanate nanorods (TNR). TNP were commercially available TiO_2 precursor (DT-51, CristalACTiV™). TNR were prepared by hydrothermal synthesis [18,19]. For this purpose, 2 g of DT-51 was dispersed in an aqueous sodium hydroxide solution (10 M). The suspension was heated at 130 °C for 24 h in a Teflon-lined autoclave. After 24 h, the resulting precipitate was separated by centrifugation and washed thoroughly several times with 0.1 M HCl and ultrapure water. The obtained material (TNR) was calcined for 2 h at 500 °C in air with a heating ramp of 120 °C per hour.

For the TNR + Au sample, the preparation procedure (wet impregnation technique) was similar to that used by Verma et al. [20]. The TNR support was ultrasonically dispersed in ethanol for 10 min, and then an Au precursor ($HAuCl_4$) was added in an amount that resulted in a metal loading of 1.0 wt%. The suspension was stirred continuously for 21 h and then evaporated using a rotary evaporator. The obtained material was dried at 80 °C for 18 h. The sample was then calcined for 2 h at 300 °C in a gas mixture of 5 % H_2/95 % N_2 with a heating ramp of 150 °C per hour [20]. The wet impregnation technique was also used in the synthesis of TNP + Au sample. Here, the TNP was added to an aqueous solution of the Au precursor and stirred for 20 h. The solution was dried at room temperature for 12 h. The next step was calcination at 300 °C for 2 h with a heating ramp of 300 °C per hour.

2.3. Catalyst characterization

The materials used in the study were analyzed using a transmission scanning electron microscope (TEM, JEM-2100, Jeol Inc.) and a scanning electron microscope (SEM, SUPRA 35 VP, Carl Zeiss) equipped with an energy-dispersive X-ray spectrometer (SEM-EDXS, Inca 400, Oxford Instruments) to determine their morphology and composition. To prepare the samples for TEM, they were briefly sonicated in ethanol, while the samples for SEM-EDXS were attached to an aluminum holder with double-sided carbon tape and then purged with a stream of air to remove any residual material. Inductively coupled plasma optical emission spectroscopy (ICP-OES) analysis was performed on the synthesized catalyst samples to determine the Au content using a Variam 715-ES ICP optical emission spectrometer.

A Micromeritics TriStar II 3020 analyzer was used to determine the structural properties by means of N_2 physisorption. Prior to the measurements, the catalysts were degassed with a Micromeritics SmartPrep unit at 90 °C for 60 min and 180 °C for 240 min with N_2 gas (purity 6.0). The specific surface area was determined using the Brunauer-Emmett-Teller (BET) method, while the Barrett-Joyner-Halenda (BJH) method was used to calculate the total pore volume and pore size distribution from desorption isotherms.

The crystallinity and phase composition of the catalysts were analyzed by powder X-ray diffraction (XRD) using a PANalytical X'Pert Pro diffractometer with Cu $K_{\alpha1}$ radiation (λ = 0.15406 nm). Scanning was performed in the 2θ range between 5 and 90°, with a step increment of 0.033°.

Zeta potential measurements of the tested materials were performed at 25 °C using Malvern Panalytical's Zetasizer Ultra (MPT-3) equipped with ZS EXPLORER software and a multipurpose titrator with 0.25 M sodium hydroxide (NaOH) and 0.25 M/0.025 M hydrochloric acid (HCl) to adjust the pH from 2 to 9.

The UV–Vis diffuse reflectance (UV–Vis DR) spectra of the analyzed catalysts were measured with a UV–Vis spectrophotometer (Perkin Elmer, model Lambda 650) equipped with a Praying Mantis, DRP-SAP accessory from Harrick. Measurements were taken at room temperature at a scan rate of 266.75 nm per minute and covered the wavelength range between 200 and 900 nm. Spectralon© was used for background correction.

A Perkin Elmer UV–Vis fluorescence spectrometer LS 55 was used to measure the photoluminescence (PL) of the solid samples. The excitation

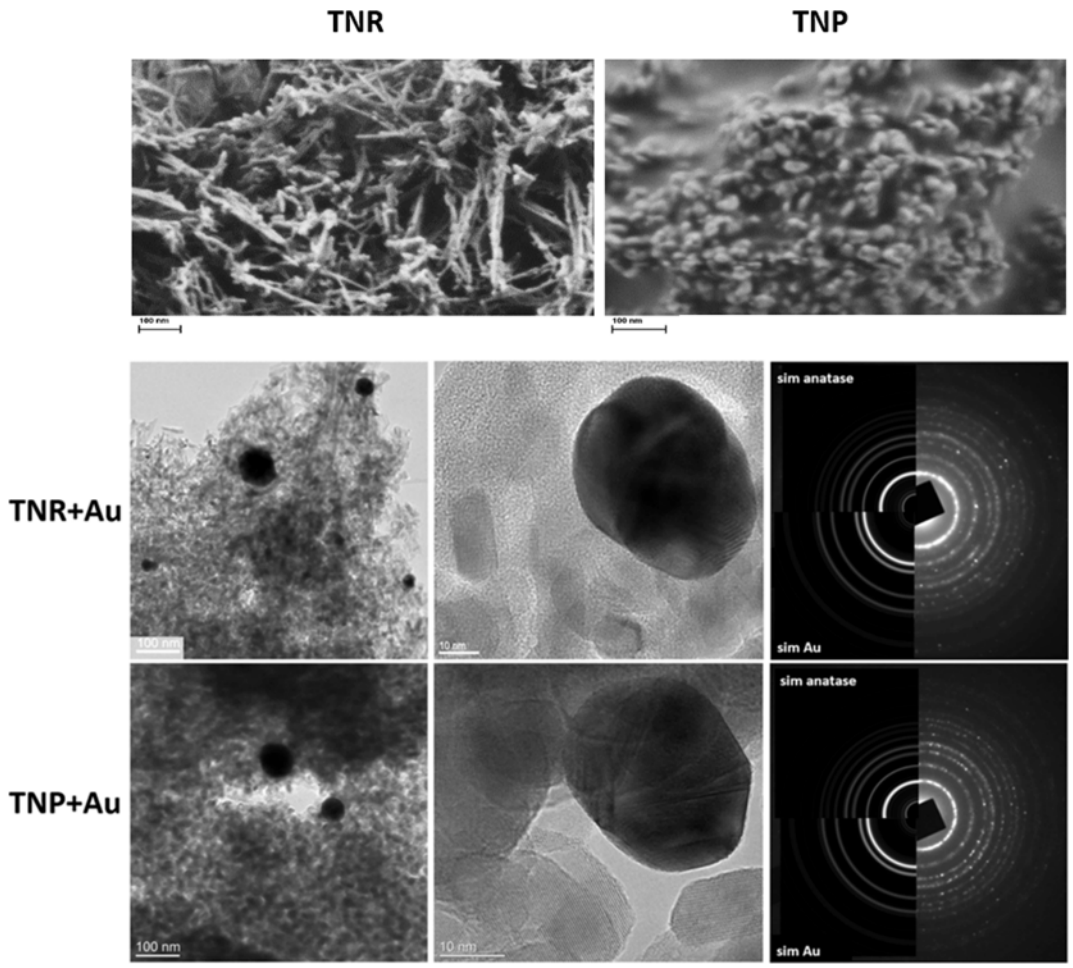

Fig. 1. SEM micrographs of TNR and TNP samples and TEM micrographs of TNR + Au and TNP + Au samples with the corresponding experimental SAED pattern. The dark spherical nanoparticles represent the Au NPs.

wavelength was set to 315 nm and the analyzed wavelength range was adjusted from 300 to 600 nm.

A Perkin Elmer FTIR spectrometer (model Frontier) was used for the ATR-FTIR measurements. Each spectrum was an average of 32 scans with a spectral resolution of 4 cm^{-1} over a range of 4000 and 400 cm^{-1}.

X-ray photoelectron spectroscopy (XPS) was used to analyze the powder samples. A Supra + device (Kratos, Manchester, UK) with an Al K_α excitation source was used for this purpose. The powder samples were attached to the carbon tape on the Si wafer. A charge neutralizer was switched on during the measurements. The spectra were recorded at a transmission energy of 20 eV and an acceptance angle of 90°. The spectra obtained were analyzed with the ESCApe 1.5 software (Kratos).

An X-band Adani CMS8400 EPR spectrometer was used to obtain the solid-state paramagnetic resonance (EPR) spectra at room temperature. Mg(II)/MgO powder was used as a standard to determine the uncertainty of the measurements. All powdered samples were filled into quartz sample tubes and inserted into the EPR spectrometer (9.4 MHz microwave frequency). The measurements were centered at 338 mT, with a sweep width of either 40 or 200 mT and a mod. amplitude of 450 μT, a power attenuation of 15 dB and a gain value of 2×10^3. The sweep time was set to 180 s and 6 scans were averaged to obtain the EPR spectra. For visible-light illumination, we used a Schott KL 2500 LED light source and irradiated the samples through the side channel of the EPR spectrometer for 15 min before measuring the spectra.

2.4. Evaluation of the photocatalytic activity

We prepared an aqueous $ABTS^{\bullet+}$ solution to measure the light-induced production of e^- and reactive oxygen species (ROS), i.e. superoxide anion radicals ($O_2^{\bullet-}$), by dissolving 17.2 mg of 2,2′-azino-bis(3-ethylbenzothiazoline-6-sulphonic acid) salt ($ABTS^{\bullet+}$) and 3.3 mg of $K_2S_2O_8$ in 5 mL of ultrapure water to monitor the formation of e^- and $O_2^{\bullet-}$ [21]. We added 10 mg of the prepared catalysts to 1 mL of $ABTS^{\bullet+}$ solution diluted in 50 mL of ultrapure water. We stirred the mixture at 400 rpm in a 100 mL glass batch reactor. The suspension was first stirred in the dark for 20 min to establish sorption equilibrium. We then switched on a Schott KL 2500 LED visible-light source and collected and filtered samples of the liquid-phase at specific time intervals. The $ABTS^{\bullet+}$ aqueous-phase samples were analyzed by measuring UV–Vis spectra (Perkin Elmer, model Lambda 465) with a TrayCell cuvette (Hellma), where we followed the decrease and increase of the $ABTS^{\bullet+}$ absorption bands at 415 and 340 nm, respectively [21].

To determine the tendency for $O_2^{\bullet-}$ generation, spin trapping experiments were performed with DMPO dissolved in DMSO as solvent. Measurements of the corresponding spin adduct (DMPO-$O_2^{\bullet-}$) were performed using a 100 μL liquid flat cell (Fluorochem, model WG-808_Q) and an Adani CMS8400 EPR spectrometer. The illumination source for the visible light in all cases was the Schott KL 2500 LED lamp. The center field was at 337.00 mT (sweep width 10 mT) with a mod. amplitude of 200 μT and a power attenuation of 15 dB (gain value of 4×10^3). The initial concentration of DMPO was 4 g/L and that of the catalyst 2 g/L, respectively. The DMSO/catalyst suspension was stirred

Table 1
Results of N_2 physisorption (S_{BET}, V_{pore} and d_{pore}), XRD (the apparent crystallite size of anatase was calculated from the diffraction peak at 25°, using the Scherrer equation), TEM (average size of Au NPs) and XPS (SBH) analyses of the investigated TNR support and TiO_2 + Au catalysts.

Sample	TNR	TNR + Au	TNP	TNP + Au
S_{BET} (m^2/g)	106	101	88	74
V_{pore} (cm^3/g)	0.48	0.45	0.31	0.29
d_{pore} (nm)	18.3	17.9	14.2	14.2
[a]Apparent anatase crystallite size (nm)	17.4	17.4	21.3	21.3
Average size of Au NPs (nm)	–	22.8	36.9	–
SBH (eV)	–	0.33	–	0.22

[a] The apparent values were calculated because the TNR support is non-spherical.

vigorously (400 rpm) and purged with air (100 mL/min) for 15 min before being used to form the DMPO/DMSO/catalyst suspension and filled into the 100 μL liquid flat cell for *in situ* measurements. TEMP in ultrapure water (18.2 MΩ cm, Purelab Flex) was used as a solvent to investigate the possible $^1O_2$ formation. The flat cell, EPR spectrometer and visible-light source were the same as in the DMPO experiments. The experiments were performed *ex situ* with a suspension of TEMP (1 g/L) and catalyst suspension (1 g/L) under stirring (400 rpm) and air flow (100 mL/min). After visible-light illumination, 50 μL of the suspension was transferred to the flat liquid cell and measured three times. For all TEMP experiments, measurements were centered at 337.00 mT (sweep width 7 mT) with a mod. amplitude of 200 μT and a power attenuation of 18 dB (gain value of 1×10^3).

An aqueous solution with a concentration of 10 mg/L BPA was used to study the process of photocatalytic degradation of this organic pollutant. The concentration was chosen according to the European Commission and the United States Environmental Protection Agency, according to which BPA is classified as toxic at the value of 1.0 to 10 mg/L [22].The BPA oxidation experiments were carried out in a 250 mL glass slurry reactor (Lenz Laborglas, model LF60) at a constant temperature of 25 °C (Julabo, model F25/ME) and atmospheric pressure. A catalyst concentration of 125 mg/L was used. The mixture of BPA and catalyst was stirred at 600 rpm during the experiment and purged with

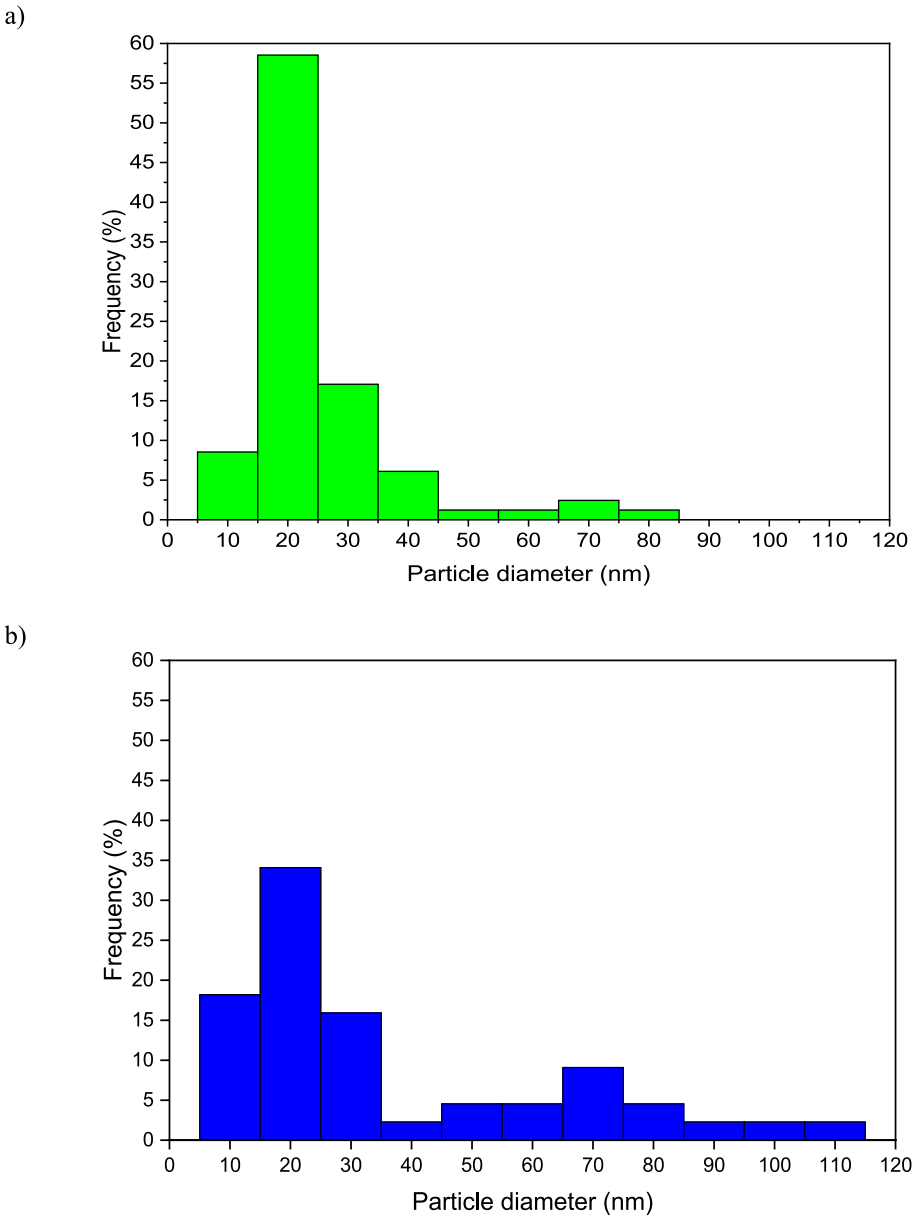

Fig. 2. Particle size distribution of Au ensembles over the TNR support in catalyst samples a) TNR + Au and b) TNP + Au.

Table 2
Results of [a]SEM-EDXS and [c]ICP-OES analysis of the investigated TNR and TNP support and TiO_2 + Au catalysts.

Sample		TNR	TNR + Au	TNP	TNP + Au
Ti	wt.%	54 ± 2.0	52.7 ± 2.4	53 ± 1.2	55.8 ± 2.0
O		46 ± 2.0	46.4 ± 2.3	47 ± 1.4	43.1 ± 2.2
[b]Au		–	0.9 ± 0.1	–	1.1 ± 0.01
[c]Au			0.92		1.03

[a] Analysis conditions: voltage 15 keV, ZAF correction method. The instrument was calibrated with an analytical mono-block from MAC.
[b] Shi et al. [63] have shown that the Au weight percentages determined by SEM-EDXS and ICP-AES analyses in TiO_2 + Au catalysts agree very well. This confirms the application of the SEM-EDXS method to evaluate the Au loading in the investigated photocatalysts. The SEM-EDXS measurements were performed in area scan mode at ten randomly selected spots.

air at a flow rate of 750 mL per minute. After a dark phase of 30 min, illumination with visible light (Philips, 150 W, λ_{max} = 520 nm) was started. To analyze the samples, the liquid-phase samples were collected and filtered through a 0.2 μm membrane filter before being analyzed using an HPLC instrument (Shimadzu, model LC-40) in isocratic mode. The column (100 × 4.6 mm BDS Hypersil C18 (2.4 μm)) was maintained at a temperature of 30 °C, and a mixture of methanol and ultrapure water (70 %: 30 %, v/v) was used as the mobile phase at a flow rate of 0.5 mL/min.

3. Results and discussion

3.1. Catalyst characterization

The nanoscale crystallites in the synthesized catalysts were analyzed using transmission electron microscopy (TEM). The microscopic images of the analyzed TNR + Au catalyst (Fig. 1) show that TiO_2 is present in the form of rod-shaped anatase nanoparticles of uniform size. The diameter of the TNR was measured to be 70 nm in length and 8 nm in width. In contrast, the TNPs have an ellipsoidal shape with a length of 30 nm and a diameter of 20 nm, whereby the crystallite phase is also anatase (SEM micrographs in Fig. 1). The microscopic TEM images also show that the Au particles in both TiO_2 + Au samples are spherical and evenly distributed over the entire surface of the TiO_2. The average size of

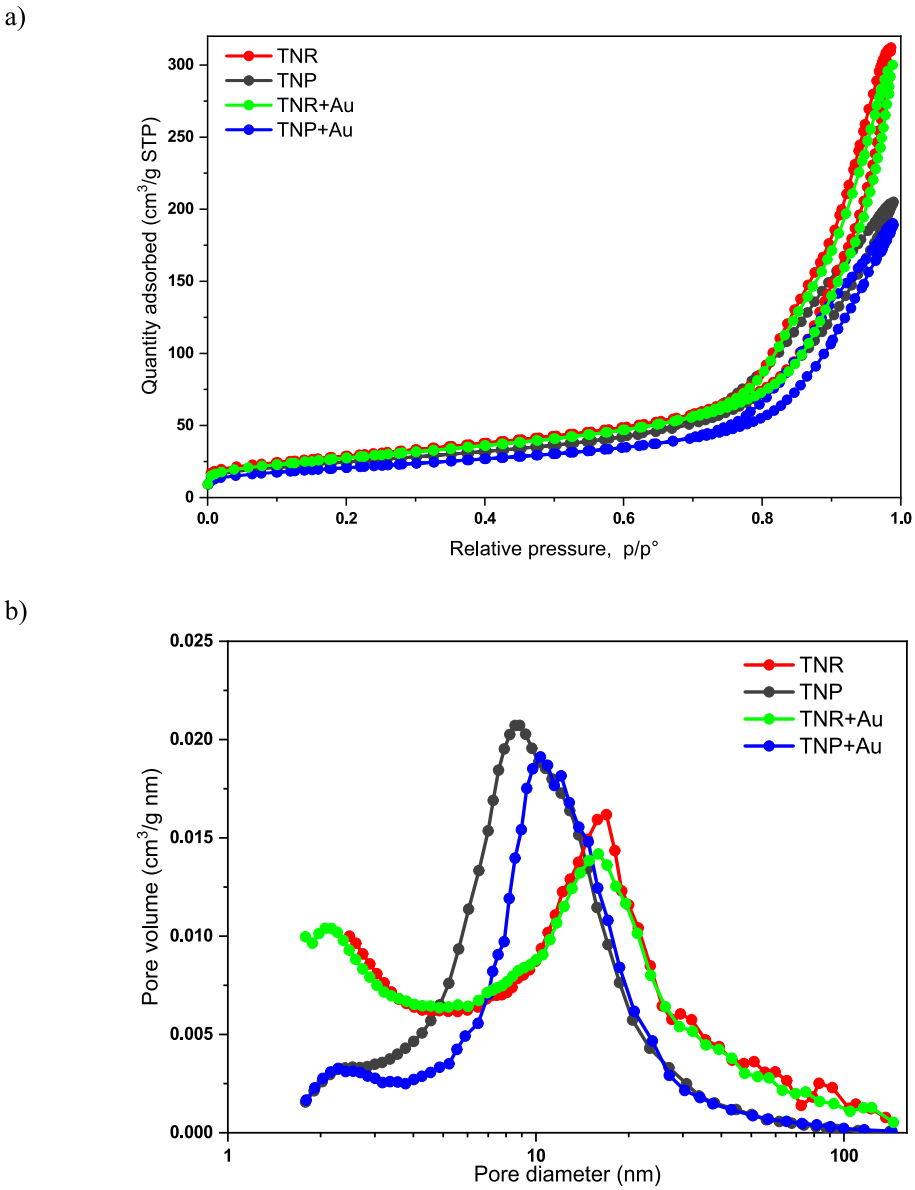

Fig. 3. a) Nitrogen adsorption/desorption isotherms and b) corresponding bjh pore size distribution for catalysts, comparing those with TNR or TNP support.

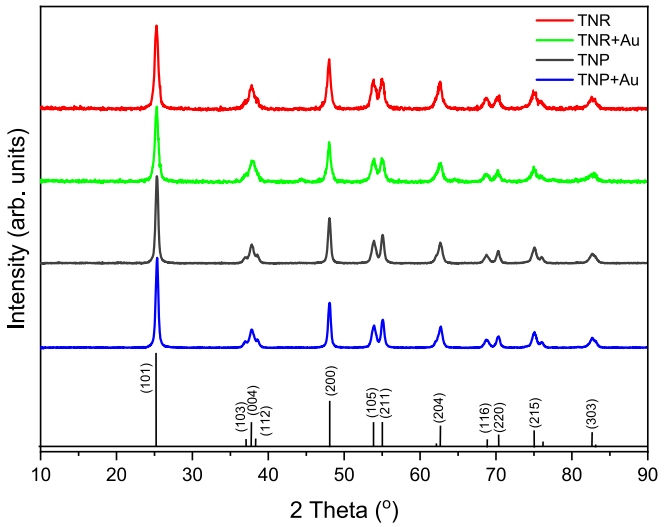

Fig. 4. XRD diffractograms of the TNR and TNP support and catalysts containing 1.0 wt% of Au loading. Solid vertical lines belong to anatase TiO_2 (JCPDS 00–021-1272).

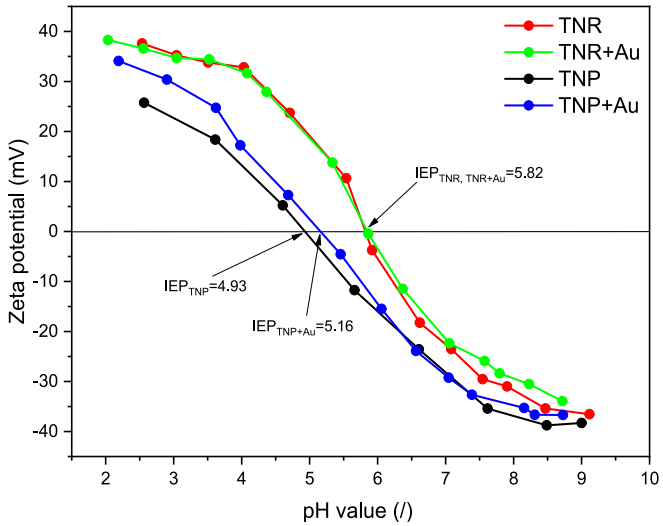

Fig. 5. The change of zeta potential depending on pH of suspension for all catalysts.

the Au particles is shown in Table 1. We measured the size of more than 100 Au particles (some of them are shown in Fig. S1) and generated the particle size distribution shown in Fig. 2. The Au sizes were calculated using the ImageJ program. In the case of the TNR + Au sample, most particles are about 25 nm in size, but smaller particles and particles up to 80 nm in size were also observed. In the case of the TNP + Au sample, most of the Au particles are also around 25 nm in size, but particles up to 110 nm in size were also found. The TNP + Au sample therefore has a wider particle size distribution (reason for this is the correlation between pH and isoelectric point (IEP), explained below) than the TNR + Au sample, but for both TiO_2 + Au samples analyzed, the majority of particles are in the same size range between 20 and 30 nm. The results of the SEM-EDXS and ICP-OES analyses (Table 2) show that the actual loading of TiO_2 with Au is very close to the nominal loading of 1.0 wt%. The EDXS analysis also proves that the sample contains only Ti, O and Au and no other Au precursor residues or impurities were present.

N_2 physisorption measurements (Fig. 3) were carried out for all analyzed materials. The results show that the specific surface area (S_{BET}), pore volume (V_{pore}) and pore diameter (d_{pore}) of TiO_2 + Au catalysts are mainly determined by the morphological properties of the TiO_2 support in both cases (Table 1), which proves that the TiO_2 supports are stable during the synthesis procedures of TiO_2 + Au catalysts and that the pores of TiO_2 supports are not blocked by Au. Naniwa et al. [23] investigated the influence of S_{BET} on the photocatalysts activity. They showed that TiO_2 photocatalysts with different S_{BET} exhibited increased activity at larger S_{BET}, although this was not uniform across all samples.

The XRD results confirm the presence of anatase TiO_2 in all four materials analyzed (Fig. 4). The anatase peaks are consistent with the standard positions documented in the literature [24]. The peak intensities remain the same for all samples, regardless of the presence of Au. This indicates that the deposition of Au does not affect the TiO_2 surface and there are no recognizable peak shifts. The uniform intensity also suggests that both TNR- and TNP-based materials have similar crystal sizes and degrees of crystallinity. The anatase crystal sizes were determined from the width of the (101) diffraction peak at 25° using the Scherrer equation. The calculated anatase crystallite size for TNR and TNR + Au samples was 17.4 nm (Table 1). However, it should be noted that this is an apparent crystallite size as the Scherrer equation is designed for spherical particles and TNR has a non-spherical morphology. For the TNP and TNP + Au samples, the anatase crystal size was determined to be 21.3 nm. This slight increase compared to TNR-based catalysts is reasonable given the inherent differences in the sizes and shapes of the catalyst bases. The lack of Au diffraction peaks in the XRD diffractograms is attributed to the fact that either the Au loading is below the detection limit of the XRD method and/or the Au crystallite size is below 10 nm and the peak is not detectable in the noise signal [25].

The zeta potential as a function of pH for the analyzed samples is shown in Fig. 5. The zeta potential decreases with increasing pH and lies between 30–40 mV and −40 mV. The IEP is the pH value of the solution at which the net charge of a catalyst surface becomes zero. In the literature, the IEP of anatase TiO_2 was found to be 6.0 [26]. IEP values of 5.82 and 4.93 were determined for the TNR and TNP support. The lower IEP value of the TNP support compared to the IEP value of the TNR support was due to the deprotonation of the TNP surface [27]. For the TiO_2 + Au samples, it is assumed that the observed differences in the IEPs are due to different synthesis procedures of the TiO_2 + Au catalysts. It should be noted that the pH of the TNR and Au precursor mixture was neutral during the synthesis of the TNR + Au catalyst, while the pH of the TNP and Au precursor suspension was acidic during the synthesis of the TNP + Au sample, which affected the size distribution of Au particles on the catalyst surface. The results obtained are in agreement with the research findings of Yazid et al. [26] who reported that the preparation of Au-containing solids at a pH below the IEP leads to the formation of larger Au particles (TEM sizes in Table 1).

The UV–Vis DR spectra of the analyzed samples are shown in Fig. 6a. To facilitate interpretation, the spectra are divided into two regions. The first region below 400 nm, the so-called UV region, shows significant light absorption in all four samples. This absorption is attributed to the presence of TiO_2, which is known for its light absorption in the UV range. The higher UV absorption observed in TNR and TNR + Au samples compared to TNP and TNP + Au solids can be attributed to differences in morphology and optical properties. In particular, the elongated structure of the nanorods improves light scattering, leading to improved absorption, as previously reported in studies on TiO_2 nanostructures [28]. Consequently, TiO_2 is only excited and catalytically active in the UV range. The measured band gap energies (Kubelka-Munk model) were determined to be 3.19 eV for the TNR sample and 3.25 eV for the TNP sample and are in good agreement with the values reported in the literature for anatase TiO_2 [29,30]. The second part of the UV–Vis DR spectra of the investigated TiO_2 + Au catalysts shows a pronounced peak in the wavelength range from 500 to 600 nm. This peak is attributed to the localized surface plasmon resonance (LSPR) effect caused by Au NPs on the surface of the TiO_2. The unique oval shape of the peak indicates

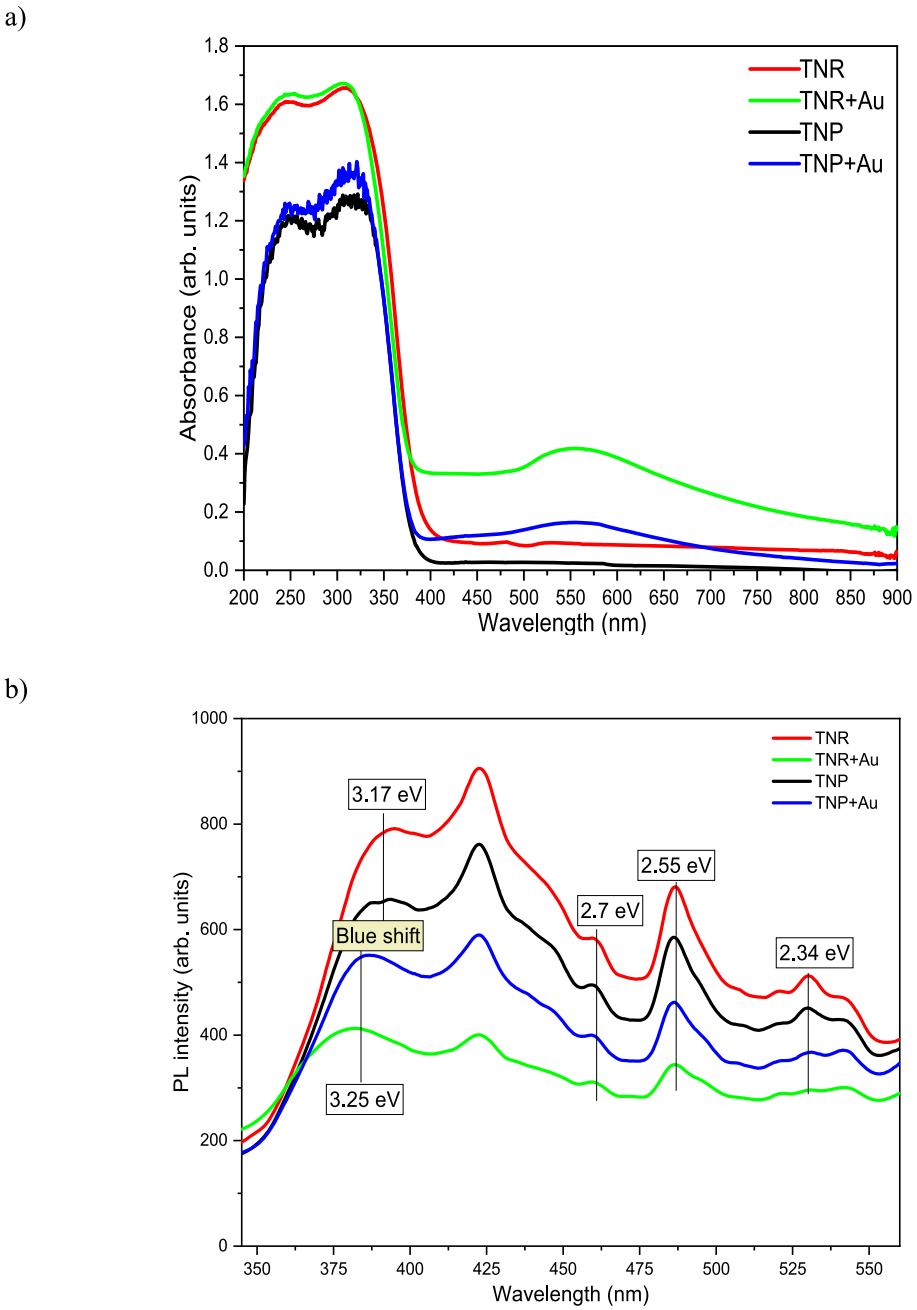

Fig. 6. a) UV–Vis DR spectra of the TNR support and catalysts containing 1.0 wt% of Au and b) solid-state photoluminescence (PL) emission spectra of the investigated materials.

that the Au NPs have a spherical morphology, a feature confirmed by TEM analysis. Remarkably, no peak shift is observed in the visible region, indicating a uniform size of the Au NPs. This uniformity is also confirmed by the particle size distribution shown in Fig. 2, which shows that the majority of Au NPs fall in the 20–30 nm range.

Photoluminescence (PL) is a non-destructive technique for analyzing semiconductors in the bulk. Since the recombination of charge carriers strongly influences the activity of the catalysts, the PL intensity of a solid used for heterogeneous photocatalysis should be low, which means a low recombination rate of charge carriers. The PL spectra of the analyzed catalysts are shown in Fig. 6b. A decrease in PL intensity is observed for the TiO_2 + Au samples compared to TiO_2, indicating the existence of an active interface between the metal and the semiconductor [31]. The peak at 3.17 eV corresponds to anatase TiO_2, while the shift to 3.25 eV in the TiO_2 + Au samples indicates a blue shift due to the suppression of indirect phonon-assisted transitions in anatase by Au. The peak at an energy of 2.9 eV represents the lowest indirect transition $\Gamma_{1b} \rightarrow X_{1a}$. The presence of Au NPs leads to fewer recombination events, which improves the photocatalytic performance. Additional peaks at 2.34, 2.55 and 2.7 eV are associated with shallow trap levels, oxygen vacancies and defects in the TiO_2 support [32]. The shallow trap levels were created by minor imperfections in TiO_2 and may arise as a defect during the synthesis process and heat treatment. The presence of oxygen vacancies states between the VB and CB in the TiO_2 structure may contribute to the appearance of the visible light absorption [32].

The measured ATR-FTIR spectra show a similar behaviour for all samples examined (Fig. S2). The absorption peaks in the 3200–3600 cm^{-1} and 1630–1660 cm^{-1} ranges are correlated with the O–H stretching vibration mode of water and the bending of water [33]. The peaks have a lower intensity in samples with Au, which is due to the

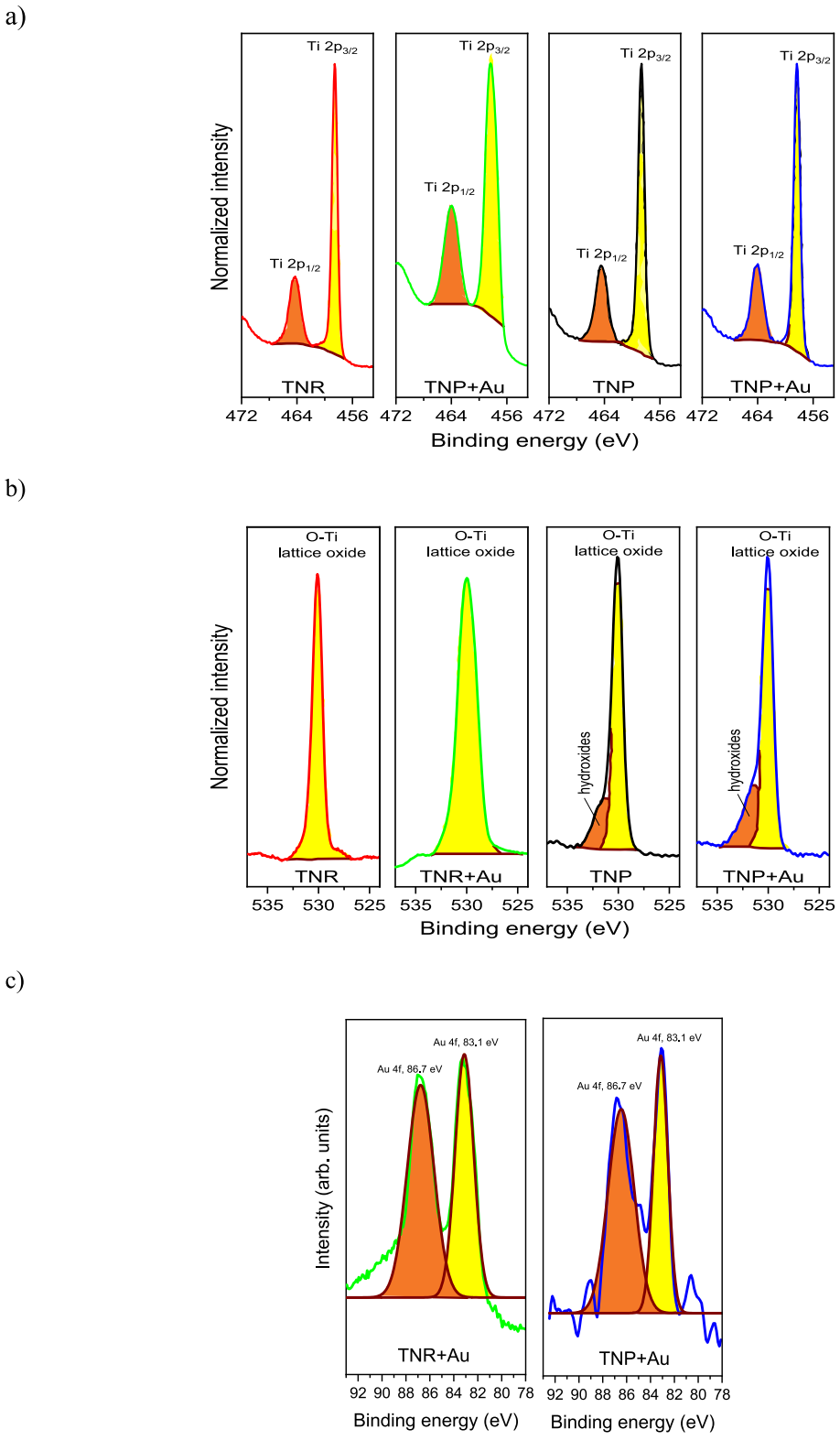

Fig. 7. Fitted a) Ti 2p, b) O 1 s and c) Au 4f spectra of catalysts.

reduction of the hydroxyl groups (Ti-OH) through the calcination process. The intensity and frequency of the IR bands in the 1250–900 cm^{-1} range are sensitive to the type of crystalline TiO_2 composition and the physically adsorbed water content [34].

The results of the XPS analysis are shown in Fig. 7, which shows the spectra of Ti 2p and Au 4f. In the case of titanium, the XPS spectra of Ti 2p are characterized by double peaks. In the spectra in Fig. 7a, two peaks appear for all samples at the binding energy 458.7 eV, representing the Ti $2p_{3/2}$ and at 464.3 eV, representing the Ti $2p_{1/2}$ states of Ti^{4+} [35]. According to the literature on the standard binding energy of Ti $2p_{3/2}$ in TiO_2, Ti^{3+} is normally at 457.7 eV and Ti^{4+} at 459.5 eV. The Ti $2p_{3/2}$ peak for samples with Au is located at 0.3 eV more negative binding energy. This could indicate that the TNR + Au and TNP + Au samples are partially reduced, with Ti^{3+} being formed [36]. The peak at 530 eV is

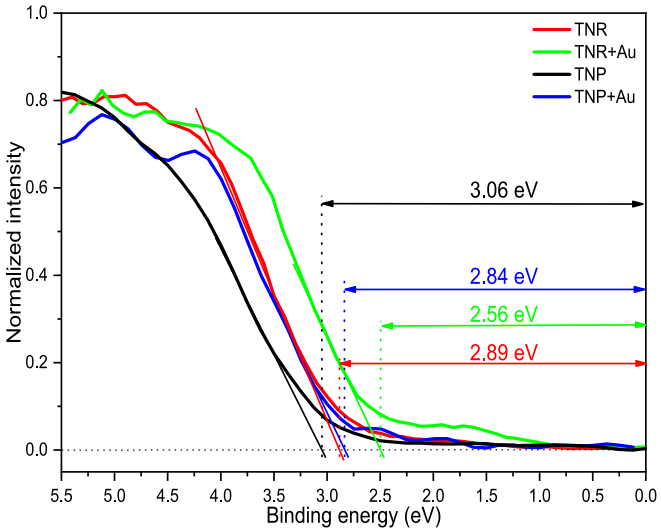

Fig. 8. Determination of VBM of pure TNR support and TiO_2 + Au catalysts using XPS analysis.

typical for the oxygen of the Ti-O bonds in TiO_2 [37], with all four peaks at a binding energy around 530 eV (Fig. 7b), which is the characteristic peak for the bulk oxide (O_2^-) in the TiO_2 catalysts [38]. In Fig. 7c we compare the Au 4f spectra of the samples TNR + Au and TNP + Au. The peaks are at 83.3 and 86.9 eV, representing Au $4f_{7/2}$ and Au $4f_{5/2}$, respectively. This could be attributed to the metallic Au(0). The Au $4f_{7/2}$ peaks were at more negative binding energies than the expected position of 84.0 eV for bulk Au (fitted spectra in Fig. 7c). It has been previously reported that the shift of the peak to more negative binding energies could be due to e^- transfer from the support to the nanoparticles [39].

The SB forms at the interface between Au and TiO_2 and monitors the transport of charge carriers at this interface. The SBH was calculated using the following equation:

$$\varnothing_{SB} = \varnothing_M - \chi \quad (1)$$

where $\varnothing_M$ stands for the work function of Au and χ for the e^- affinity of the TNR catalyst support. The SBHs were listed in Table 1. The SBH for the TNR + Au sample was 0.33 eV and for the TNP + Au catalyst 0.22 eV (Fig. 8). The TNR + Au sample with the smaller average Au NPs had a higher SBH. The SBH values in both cases were between 0.1 and 1.0. The lower SBH value for the TNP + Au sample was attributed to the high density of oxygen vacancies in TiO_2 due to the amorphous structure [40].

To elucidate the different photocatalytic behavior of TNR + Au and TNP + Au photocatalysts, we performed EPR solid-state measurements at room temperature. For pure TNP (Fig. 9a), we can observe the characteristic signals corresponding to Ti^{3+} ions (P1) and an indication of O-vacancies (P2) [41]. The calculated g-values (Table S1) are slightly higher than expected [41], which could be due either to the delocalization of the unpaired e^- or to the settings of the instrument used. In addition, we observe a possible rhombic signal for O_2^- species (P3(g2)) or oxygen-centered h^+-trapping at the surface [41–44]. As can be seen, the P1(g1⊥) and P2 signals are merged (superimposed) due to the partial heterogeneity of the sample and the instrumental limitation. In addition, pure TNP support probably contains only a small amount of O-vacancies, making them difficult to detect at room temperature. However, from the shape of the peak, it can be concluded that the Ti^{3+} species are mostly internal [45]. This is also reflected in the P5 and P6 signals, which correspond to the internal Ti^{3+} of the particles [42,44]. Another possibility is that the peaks correspond to Ti cations located at crystallization defects or substitutional Ti^{3+} in hydrated anatase [43]. Since the shape of the P1(g1⊥) signal indicates the presence of internal Ti^{3+}, we can probably also assign the P5 and P6 signals to the same species. In addition, we observe the S1 signal originating from a low sulfur content from the manufacturer's synthesis procedure [46]. The addition of Au NPs (TNP + Au sample) changes the shape of the EPR spectra compared to pure TNP. Firstly, we can now clearly observe the presence of O-gaps (P2) and increased P1(g1⊥), P5 and P6 signals for Ti^{3+}. This indicates that the impregnation of Au NPs on the TNP support generates more Ti^{3+} and O-vacancies and thus more defect sites. The shape still suggests that most of the Ti^{3+} is in the bulk, but some amount could also be present on the surface of TiO_2 [45,47]. What we also observe is the absence of the

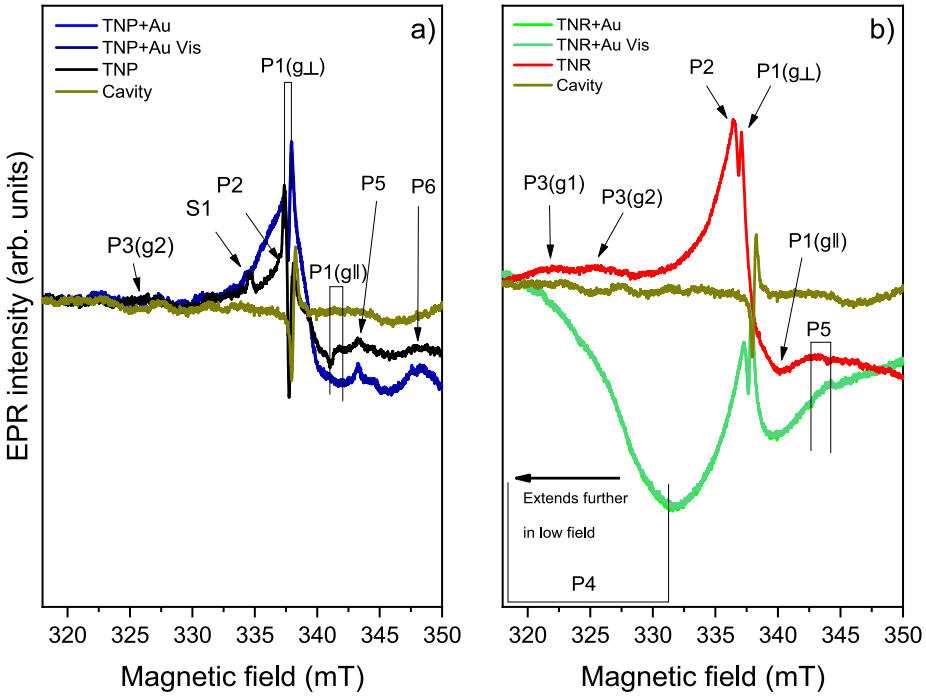

Fig. 9. Solid-state room-temperature EPR spectra of a) TNP + Au and b) TNR + Au photocatalysts under dark and illuminated conditions.

S1 peak. This can either be due to the overlapping of the peaks or the impregnation method has removed the sulfur impurities. On the other hand, impregnation with Au NPs does not change the P3 peak. Another observation is the slight decrease in the g-values for the P1 and P2 signals in the TNP + Au sample compared to pure TNP. This indicates that the unpaired e^- responsible for the EPR signal are more localized. Since the addition of Au NPs creates defects and their presence causes a disturbance in the charge migration, the electrons could localize around the Au NPs. Since the Au NPs are probably connected to the support via the Ti^{3+} and O-vacancies (defects), the e^- are localized there. Therefore, we can observe the slight decrease in the g-values for the P1 and P2 signals. The illumination with visible light does not change the EPR spectra because the thermal effect at room temperature does not allow the observation of carrier generation.

Interestingly, the TNR + Au photocatalyst generates different EPR signals than the TNP + Au photocatalyst. Fig. 9b also shows that the pure TNR support has an EPR spectrum that differs from the EPR spectrum of the TNP support. In particular, the P1 + P2 peaks are broader, indicating that most of the Ti^{3+} is located on the surface of the TiO_2 [41,47]. However, we still observe the P5 signal, which confirms the presence of internal Ti^{3+}. This is due to the hydrothermal synthesis of TNR from TNP, which generates O-vacancies on the surface. Thus, to achieve charge neutrality, additional surface Ti^{3+} is generated. The presence of surface Ti^{3+} on the TNR support was also confirmed by the high-resolution Ti 2p spectra (XPS analysis). Moreover, the S1 peaks are not present as the sulphur impurities were removed by the hydrothermal treatment. For the pure TNR support, we now also observe the P3(g1) signal, in addition to the P3(g2) signal that we observed in the EPR spectrum of the TNP support. The addition of Au NPs also has a profound effect in the case of the TNR + Au photocatalyst. What we observe first is the decrease of the peak belonging to the O-vacancies and the loss of the Ti^{3+} sites on the surface as the peak intensities change. This indicates that the Au NPs interact with the Ti^{3+} at the O-vacancies and form a close contact, and that the internal Ti^{3+} content increases. This is different from the case of the TNP + Au photocatalyst, where the impregnation method introduces O-vacancies. We did not observe any significant changes in the g-values compared to the pure TNR support, indicating that the impregnation of Au NPs does not affect e^- delocalization. The reason for this could be the new signal P4, which spread over the measurement range and masked the slight changes in properties. In order to measure this new peak completely, we had to extend the measurement range (Fig. S3). As can be seen in Fig. 8a, the TNP + Au sample does not contain any new signals in this extended measurement range. However, the new signal (P4) for the TNR + Au sample has a g-value of approx. 2.266 (maximum at approx. 299 mT) and a line width of 33.2 mT. The corresponding Ti^{3+} and O-vacancies signals remain intact and overlap with the new P4 peak. The overwhelming intensity and shape suggest that we are indeed measuring the ferromagnetic resonance [48,49] of Au NPs, which likely originates from reduced Au centers from the $HAuCl_4$ precursor, namely Au^0 ($[Xe]4f^{14}5d^{10}6s^1$) and/or Au^{2+} ($[Xe]4f^{14}5d^9$) [50]. Since the XPS results indicate that only Au^0 is present, we can assume that no or little Au^{2+} is present and that the corresponding signal originates from the Au^0 species [51]. For Au NPs to exhibit ferromagnetic or superparamagnetic behaviour, spin–orbit coupling and crystal distortion are important parameters; other properties must also be appropriate. In particular, the magnetic behaviour depends on the dimensions of Au at the atomic level and the charge state [52]. If all properties are correct, a few crystals can undergo a physical reorientation due to an applied field and exhibit low ferromagnetic properties. If the quantity is large enough, this can even be observed at room temperature [53], as we have done. That the Au NPs in the case of the TNR + Au photocatalyst might have suitable properties for a magnetic response could be concluded from the lower SBH (0.22 eV) than in the case of the TNP + Au sample (0.33 eV). Another aspect is that the TNR + Au photocatalyst also contains non-functionalized Au NPs, which are only a few nm in size (1–5 nm, TEM hysteresis) and are known for a possible intrinsic ferromagnetic behavior [52,54]. Since we can observe this phenomenon even at room temperature, we can conclude that we have a sufficiently high amount of atypical Au NPs in the TNR + Au sample. This is consistent with the UV–Vis DR measurements where we observe the highest LSPR "hump", indicating a more intense LSPR effect in the TNR + Au sample. Since this effect is related to the size and number of suitable Au NPs susceptible to the quantum effect, we can tentatively conclude that a large amount of atypical Au NPs are indeed present in the TNR + Au sample. From the shape and width of the P4 signal, we can further infer that it resembles systems with ferromagnetic interactions, suggesting the occurrence of structural defects [55–57]. Similar to the intrinsic ferromagnetism of Fe ions, the interaction of AuNP across F-color centers (i.e., O-vacancies) could generate the strong ferromagnetic signal (P4) due to the emergence of magnetic ordering over short distances [49]. The width of the signal could indicate that the magnetic properties are due to dipole–dipole interactions, which dominate over the exchange interactions in the dark because they are superimposed on the Zeeman interactions. If the exchange interactions were dominant, we would observe a decrease in linewidth as they average the local magnetic fields around the centers [58]. Since we observed a decrease in the signal for O-vacancies in the TNR + Au sample compared to the pure TNR support, this could indicate that the Au NPs are indeed interacting with these centers. However, we have to say that the Au NPs on the TNR can be considered as defects/disorders of e^- delocalization in the TNR support. When illuminated with visible light, the intensity of the P4 peak remains the same, similar to the TNP + Au photocatalyst. Again, this is probably due to the overwhelming thermal effect at room temperature, which masks the photogeneration of e^-. Another possibility would be that the TNR + Au sample could not generate e^- under illumination due to the different properties of the Au NPs; however, we observed the LSPR effect in the UV–Vis DR measurements, which means that the thermal explanation is likely the correct one.

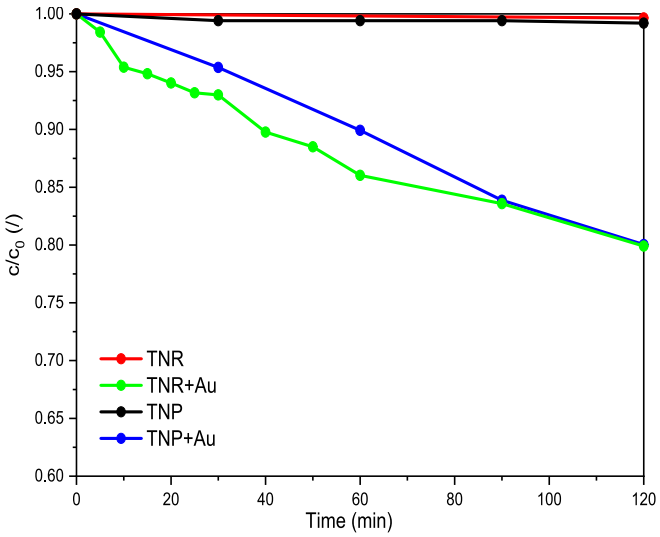

Fig. 10. Relative concentration of $ABTS^{\bullet+}$ as a function of time obtained in the presence of investigated photocatalysts under visible-light illumination.

3.2. Evaluation of the photocatalytic activity

In the $ABTS^{\bullet+}$ reaction we measured the production of e^- and the formation of $O_2^{\bullet-}$. Fig. 10 shows the relative concentration of the $ABTS^{\bullet+}$ cation as a function of time under visible-light illumination. The trend of $ABTS^{\bullet+}$ reaction was similar for the samples without Au, TNR and TNP. For these two samples, no e^- and $O_2^{\bullet-}$ generation was observed under visible light. The trend was also the same for the TNR + Au and TNP + Au samples, independently of size of catalysts support. The consumption

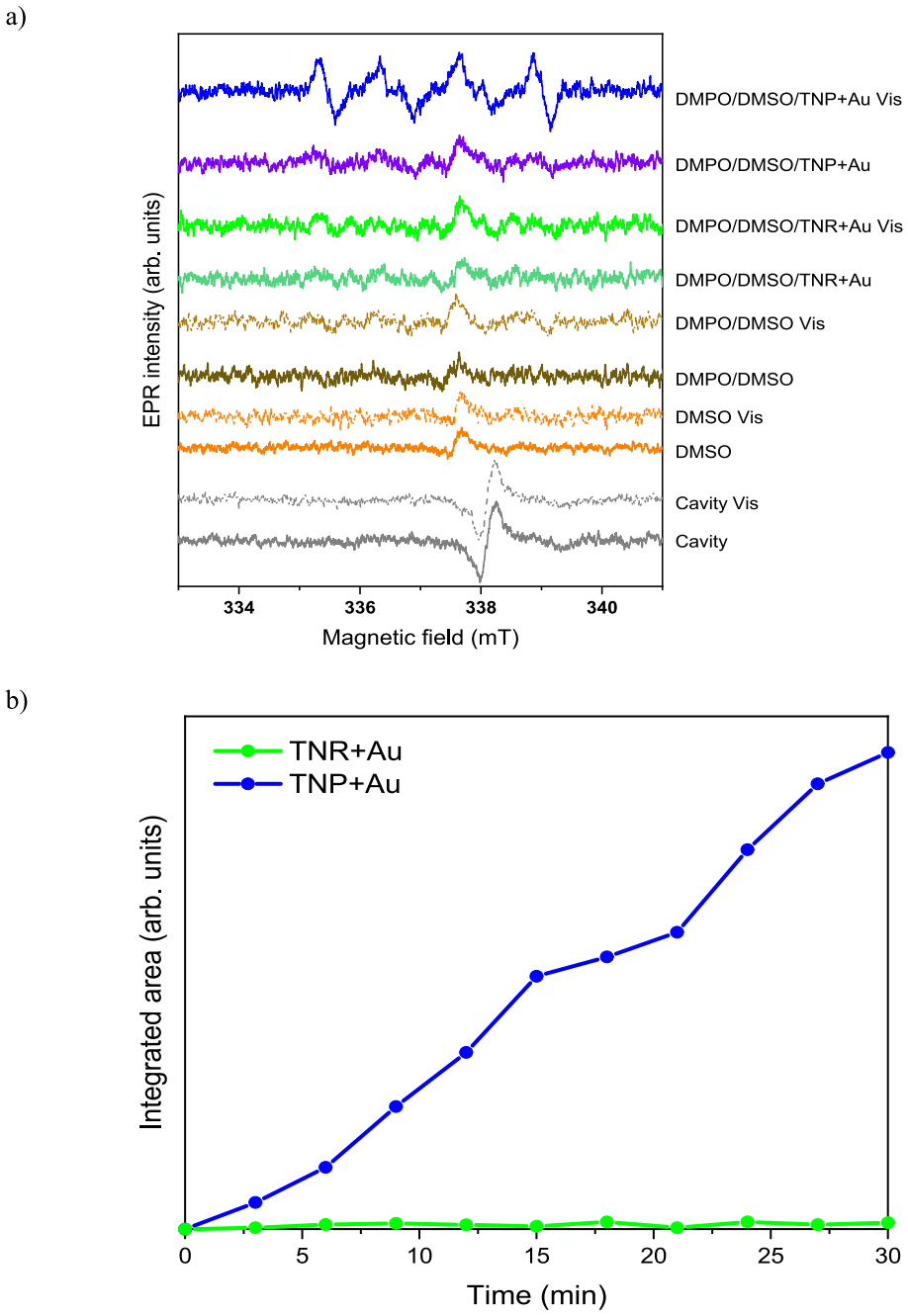

Fig. 11. a) DMPO/DMSO/catalyst results of liquid-phase epr measurements for pure DMSO, DMPO/DMSO and dmpo/dmso/catalyst suspension in the dark and after 30 min of visible-light illumination; b) Graphical representation of the double-integrated area of EPR spectra vs. time of visible-light illumination for TiO_2 + Au photocatalysts.

of $ABTS^{\bullet+}$ was low, indicating that not many $O_2^{\bullet-}$ radicals were formed in the presence of these catalysts under visible-light illumination. Based on the results shown in Fig. 10, one would expect both TiO_2 + Au photocatalysts to have the same activity for BPA degradation; however, as explained below, this was not the case.

Since in the case of the $ABTS^{\bullet+}$ scavenging experiments both e^- and $O_2^{\bullet-}$ are responsible for the reduction of the $ABTS^{\bullet+}$ complex, we performed the EPR spin-trapping analysis to distinguish between the active species. Using DMSO as a solvent, we stabilized the $O_2^{\bullet-}$ species and formed the DMPO-$O_2^{\bullet-}$ adduct (1:1:1:1 quartet). As can be seen in Fig. 11a, the TNR + Au catalyst does not generate a signal for the DMPO-$O_2^{\bullet-}$ adduct. On the other hand, the TNP + Au photocatalyst shows the formation of the DMPO-$O_2^{\bullet-}$ adduct, measured after 30 min of irradiation with visible light. The width of the peaks can be attributed to the DMPO-OCH_3 adduct formed by the reaction with the solvent (DMSO) under visible-light illumination, or to the interactions of O_2 with DMPO-$O_2^{\bullet-}$ [59]. The difference between TNR + Au and TNP + Au materials can be seen even more clearly in Fig. 11b, where the area obtained by double integration of the EPR spectra is plotted against the illumination time. The TNP + Au photocatalyst shows a steady increase in the DMPO-$O_2^{\bullet-}$ adduct formed over time. However, the TNR + Au photocatalyst does not generate an EPR signal at either illumination time point or it is at least below the detection limit. The reason for this could be the higher SBH in the case of the TNR + Au photocatalyst (0.33 eV) compared to the TNP + Au photocatalyst (0.22 eV). As a consequence, in the case of the TNR + Au material, the SBH is too high for the photogenerated e^- to

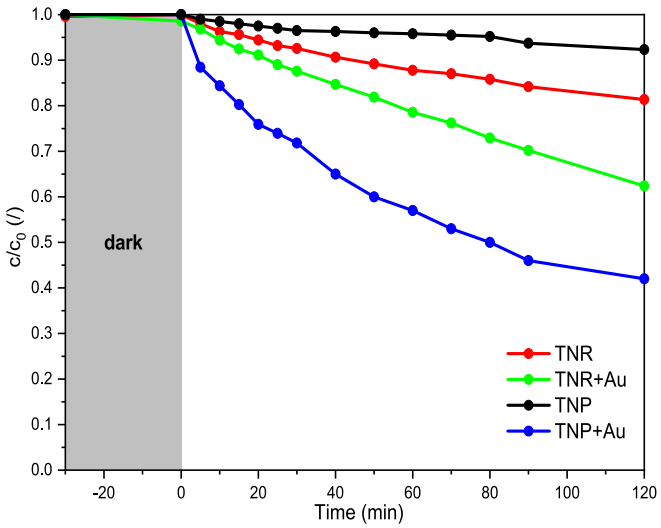

Fig. 12. Photocatalytic degradation of BPA dissolved in water ($V = 250$ mL, $c_0 = 10.00$ mg/L) under visible-light illumination obtained at $T = 25$ °C in the presence of pure TNR and TNP supports and TiO_2 + Au catalysts (125 mg/L).

jump into the CB of the TNR, and they remain in the Au NPs. On the other hand, the lower SBH of the TNP + Au material is favourable for the injection of e^- into the CB of TNP. This means that the TNP + Au photocatalyst can form $O_2^{\bullet-}$ under visible-light illumination and that both e^- and $O_2^{\bullet-}$ are responsible for its $ABTS^{\bullet+}$ reduction. From the facts described above, it can also be concluded that the oxygen reduction reaction takes place predominantly on the surface of the TiO_2 support.

The photocatalytic oxidation of the model pollutant BPA dissolved in water took place in the glass reactor with constant stirring and air purging. Fig. 12 illustrates the results of the reaction and shows the change in relative concentration as a function of time. The first 30 min of the reaction took place without illumination to investigate the adsorption of BPA on the catalyst surface. During this dark period, the BPA concentration remained constant in all four catalyst samples, indicating a lack of BPA adsorption. As a lack of BPA adsorption and photolysis, the experiment without illumination and photocatalyst was done as a proof of the concept (Fig. S4). The degradation of BPA in the presence of TNR and TNP supports was minimal, which can be attributed to the presence of Ti^{3+} species on the surface and surface defects. In particular, the hydrothermally synthesized TNR material showed more surface defects compared to the commercial TNP, indicating that it is better able to degrade the pollutant BPA. The catalysts TNR + Au and TNP + Au degrade BPA more strongly compared to the TNP and TNR samples. It follows that the addition of Au to the surface increases the photocatalytic activity. However, the BPA degradation over the TNP + Au sample is higher (almost 60 %), which also shows a higher efficiency in the EPR measurements. In contrast, the BPA degradation achieved in the presence of the TNR + Au sample is only 40 %. Based on the S_{BET} results, a higher degradation would be expected in the presence of the TNR + Au catalyst. However, since S_{BET} is not the only factor determining photocatalytic activity, other factors, such as SBH, are crucial. The higher SBH in the TNR + Au sample can lead to inefficient charge transfer, while in the TNP + Au solid a more favorable SBH promotes increased photocatalytic activity.

EPR results prove that the BPA degradation in the case of the TNR + Au photocatalyst must be due to the interaction of e^- with the BPA molecule, in addition to the small amount of $OH^{\bullet}$ radicals formed from the h^+ in TNR. In agreement with the scavenging and spin-trapping experiments, we propose the charge carrier mechanism presented in Fig. 13, which differs for both photocatalysts. The TNP + Au material exhibits a straightforward mechanism. Since the TNP component does not produce charge carriers and a narrow interface is formed between TiO_2 and Au NPs [19], the generated hot e^- of Au NPs can be injected into CB of TNP as the SBH is suitable. The hot e^- in the CB of TNP can first generate $O_2^{\bullet-}$ (oxygen reduction reaction), which can attack BPA directly, or indirectly form $OH^{\bullet}$ radicals, which attack BPA. Since both ROS are quite strong, this explains the high BPA degradation under visible-light illumination. On the other hand, the TNR + Au photocatalyst behaves differently, even though the basic chemistry (TiO_2 + Au) is the same. As can be seen in Fig. 6b, the TNR + Au photocatalyst exhibits the lowest PL signal of all materials, which means that it has the lowest tendency for radiative recombination of charge carriers. This indicates that the photogenerated e^- and h^+ could still be utilized to degrade organic pollutants even if they do not form $O_2^{\bullet-}$. This is probably possible due to the different properties of Au NPs in the examined photocatalysts. The LSPR effect (Fig. 6a) shows a slightly higher intensity ("hump") in the case of TNR + Au sample, which could indicate a higher amount of LSPR-capable Au NPs. Since the TNR + Au photocatalyst does not form $O_2^{\bullet-}$, it requires a large amount of formed charge carriers (e^-) to achieve the degradation of organic pollutants ($ABTS^{\bullet+}$ reduction). The TNR + Au catalyst have a larger surface area available for distribution, which

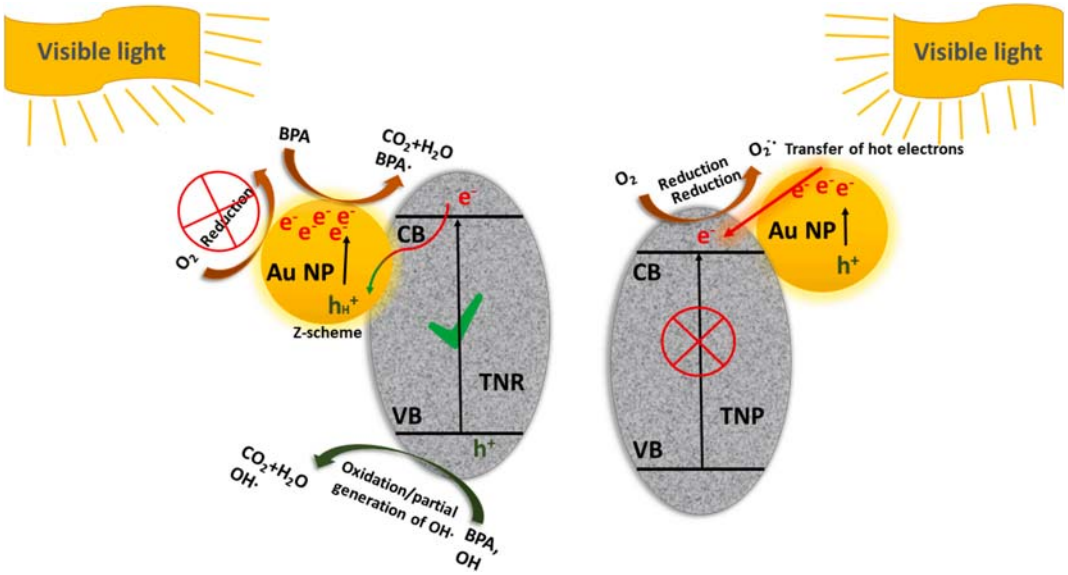

Fig. 13. The proposed charge carrier mechanism for TNR + Au and TNP + Au photocatalysts under visible-light illumination.

results in good charge separation. The generation of charge carriers in the TiO_2 component (TNR) is also a plus, as it contains small amounts of Ti^{3+}, which can utilize visible light.

The energy band distribution of catalysts is important for their effectiveness. For the TNR support, the CB potential is −0.3 eV and the VB potential is 2.89 eV, while for the TNP support the calculated CB potential is −0.19 eV and the VB potential is 3.06 eV. After impregnation, the trend is similar for the TiO_2 + Au supported catalysts. For the TNR + Au sample, the CB potential is −0.59 eV and the VB potential is 2.56 eV, and for the TNP + Au sample, the CB potential is −0.36 eV and the VB potential is 2.84 eV. The standard reduction potential for the redox pair $O_2/O_2^{\bullet-}$ in aqueous media is −0.16 eV [60]. From the latter data, the logical conclusion would be that the TNR + Au catalyst is more active, since the CB potential is more negative than the $O_2/O_2^{\bullet-}$ potential, and therefore the oxygen reduction reaction should be faster compared to the TNP + Au catalyst. However, in our case, the oxygen reduction reaction only takes place in the case of the TNP-supported Au catalyst, which means that the energy bands of the materials do not play a decisive role. The reason for the better activity of the TNP + Au catalyst is therefore most likely due to the difference in SBH. Since we have not observed any generation of $O_2^{\bullet-}$ in the TNR + Au material and the SBH is quite high (0.33 eV), we can tentatively assume that the E_{Fermi} of Au NPs (location of hot holes (h_H^+)) and CB of TNR are appropriately aligned, which enabled the "Z-scheme" to take place [61]. Due to the high SBH, some e^- cannot be extracted to the TiO_2, but recombine predominantly with h_H^+ within the Au NPs. Such recombination is intrinsic to plasmonic systems and is widely recognized as one of the key factors limiting the efficiency of hot carrier utilization [62]. However, as the Ti^{3+} content in the TNR support is still low, the concentration of the generated e^- is estimated to be low, which limits the effectiveness of the "Z-scheme". This term is used in a broader sense to describe the plasmon-mediated transfer of hot carriers, which is similar to the directional flow of charges in a "Z-scheme": i) energetic hot e^- generated in Au can overcome the SB and transfer to the conduction band of TiO_2 and ii) the h_H^+ left in Au can recombine with e^- from the valence band of TiO_2, completing the cycle. This plasmon-mediated process mimics the "Z-scheme" in terms of charge flow and redox reaction enhancement.

The photogenerated h^+ remaining in the VB of TNR support can form $OH^\bullet$ radicals, which attack the BPA molecule. The formation of $OH^\bullet$ radicals for the pure TNR support and the TNR + Au photocatalyst was observed in the COUM scavenging experiments (Fig. S5). These experiments also support the assumption of the "Z-scheme", as the formation of $OH^\bullet$ radicals was only slightly increased for the TNR + Au photocatalyst compared to the pure TNR support. This is probably due to the partial "Z-scheme" mechanism, which allows better utilization of h^+ in the VB of the TNR support. Since the properties of the TNR + Au photocatalyst are not favourable for the formation of $O_2^{\bullet-}$, the $OH^\bullet$ radicals generated by the h^+ in the VB of the TNR support (minority) and the e^- in the Au NPs (majority) attack the BPA and form radical intermediates that further degrade the organic compounds. Since the e^- are less potent than $O_2^{\bullet-}$ or $OH^\bullet$ radicals, the TNR + Au photocatalyst performs photocatalytically worse than the TNP + Au photocatalyst, which can generate $O_2^{\bullet-}$. However, in reactions in which e^- play the decisive role, the TNR + Au photocatalyst would probably perform better than the TNP + Au material.

The change in the expected BPA photooxidation activity of the TNR + Au sample can also be explained by the different properties of the Au NPs, i.e. the ferromagnetic character of the Au NPs. This affects the mechanism of charge carrier transfer, so that the TNR + Au photocatalyst performs worse than the TNP + Au photocatalyst, which has the correct Au NPs properties for the reaction under investigation. The main improvement from the addition of Au NPs in the TNR + Au photocatalyst is probably the improved charge separation in the TNR support, which allows a higher generation of $OH^\bullet$ radicals than in pure TNR, enabled by the Ti^{3+} present in the TNR support. Since the Au NPs have different properties, the e^- generated by LSPR cannot reduce the oxygen to $O_2^{\bullet-}$ (DMPO/DMSO), but they can attack the BPA molecule directly, as seen in the $ABTS^{\bullet+}$ experiments (utilization of the e^-). However, this limits the overall activity of the TNR + Au photocatalyst, although some properties (S_{BET}, energy band distribution) indicate a potentially higher activity compared to TNP + Au sample. The decisive factors were the BPA degradation pathway (mainly via $O_2^{\bullet-}$) and the excessively high SBH value, which hinders the formation of $O_2^{\bullet-}$ radicals on the TNR + Au catalyst.

4. Conclusions

In this study, we investigated two TiO_2-based Au catalysts deposited on TNR and TNP. The TNR were prepared from commercially available TiO_2 (TNP) by hydrothermal synthesis. In both cases, the Au NPs were deposited on the TiO_2 surface by wet impregnation with a longer mixing time. For both synthesized catalysts, the maximum size of the Au particles was in the range of about 20–30 nm. All characterizations confirmed the differences between the two TiO_2 + Au catalysts, indicating that the shape of the TiO_2 is important.

Degradation of BPA dissolved in water took place under visible-light illumination, with both TNR and TNP supports showing some activity, which is due to the defects being more numerous on the surface of the TNR support. The photocatalytic tests with the TiO_2 + Au samples showed large differences in BPA degradation. From the results of the formation of ROS in the $ABTS^{\bullet+}$ reaction, we can conclude that the formation of e^- and $O_2^{\bullet-}$ is very similar for both catalysts. Larger differences were observed in the EPR spin trapping analysis, where the results indicated that $O_2^{\bullet-}$ is an important ROS for BPA degradation in the case of the TNP + Au catalyst. For the TNR + Au photocatalyst, the DMPO/DMSO spin-trapping experiments have shown that it cannot produce $O_2^{\bullet-}$ via the oxygen reduction reaction due to the unsuitable SBH and the inappropriate properties of the Au NPs, but it can produce e^- as it reduces $ABTS^{\bullet+}$. This means that $O_2^{\bullet-}$ is not involved in the process of liquid-phase BPA degradation in the presence of this solid. It has been shown that visible-light triggered BPA degradation in the case of the TNR + Au photocatalyst occurs via the interaction of e^- in the Au NPs with the BPA molecule, in addition to the small amount of $OH^\bullet$ radicals formed by the h^+ in the VB of the TNR support, which leads to the formation of radical intermediates that further degrade the organic compounds.

The results obtained underline the importance of comprehensive characterization techniques to elucidate the complex relationships between catalyst structure, composition and catalytic activity. Through a better understanding of the mechanisms underlying pollutant degradation, our study contributes to the development of more efficient and customized photocatalytic materials for environmental remediation.

CRediT authorship contribution statement

Špela Slapničar: Writing – original draft, Visualization, Methodology, Investigation. **Gregor Žerjav:** Writing – review & editing, Visualization, Investigation. **Matevž Roškarič:** Writing – original draft, Visualization, Investigation. **Janez Zavašnik:** Writing – review & editing, Visualization, Investigation. **Albin Pintar:** Writing – review & editing, Supervision, Resources, Methodology, Funding acquisition, Conceptualization.

Declaration of competing interest

The authors declare that they have no known competing financial interests or personal relationships that could have appeared to influence the work reported in this paper.

Acknowledgments

The authors acknowledge the financial support from the Slovenian Research and Innovation Agency (research core funding No. P2-0150).

The authors thank Prof. Janez Kovač (Jožef Stefan Institute, Ljubljana, Slovenia) and Prof. Matjaž Finšgar (University of Maribor, Slovenia) for carrying out XPS analyses.

Appendix A. Supplementary data

Supplementary data to this article can be found online at https://doi.org/10.1016/j.apsusc.2025.162923.

Data availability

Data will be made available on request.

References

[1] C.B. Anucha, I. Altin, E. Bacaksiz, V.N. Stathopoulos, Titanium dioxide (TiO_2)-based photocatalyst materials activity enhancement for contaminants of emerging concern (CECs) degradation: In the light of modification strategies, Chem. Eng. J. Adv. 10 (2022) 100262.

[2] N.S. Allen, N. Mahdjoub, V. Vishnyakov, P.J. Kelly, R.J. Kriek, The effect of crystalline phase (anatase, brookite and rutile) and size on the photocatalytic activity of calcined polymorphic titanium dioxide (TiO_2), Polym. Degrad. Stab. 150 (2018) 31–36.

[3] S.J. Smith, R. Stevens, S. Liu, G. Li, A. Navrotsky, J. Boerio-Goates, B.F. Woodfield, Heat capacities and thermodynamic functions of TiO_2 anatase and rutile: Analysis of phase stability, Am. Mineral. 94 (2009) 236–243.

[4] M. Synoiec, A. Micek-Ilnicka, K. Szczepanowicz, A. Różycka, A. Trenczek-Zajac, K. Zakrzewska, M. Radecka, Functionalized structures based on shape-controlled TiO_2, Appl. Surf. Sci. 473 (2019) 603–613.

[5] N. Sobti, A. Bensouici, F. Coloma, C. Untiedt, S. Achour, Structural and photoelectrochemical properties of porous TiO_2 nanofibers decorated with Fe_2O_3 by sol-flame, J. Nanopart. Res. 16 (2014) 2577.

[6] Y. Li, X. Wei, B. Zhu, H. Wang, Y. Tang, T. Chen Sum, X. Chen, Hierarchically branched Fe_2O_3@TiO_2 nanorod arrays for photoelectrochemical water splitting: facile synthesis and enhanced photoelectrochemical performance, Nanoscale 8 (2016) 11284–11290.

[7] R. Katal, S. Masudy-Panah, M. Tanhaei, M.H.D.A. Farahani, H. Jiangyong, A review on the synthesis of the various types of anatase TiO_2 facets and their applications for photocatalysis, Chem. Eng. J. 384 (2020) 123384.

[8] V.C. Thipe, A.R. Karikachery, P. Çakilkaya, U. Farooq, H.H. Genedy, N. Kaeokhamleod, D.H. Phan, R. Rezwan, G. Tezcan, E. Roger, K.V. Katti, Green nanotechnology-An innovative pathway towards biocompatible and medically relevant gold nanoparticles, J. Drug Deliv. Sci. Technol. 70 (2022) 103256.

[9] M.R. Khan, T.W. Chuan, A. Yousuf, M.N.K. Chowdhury, C.K. Cheng, Schootky barrier and surface plasmonic resonance phenomena towards the photocatalytic reaction: study of their mechanisms to enhance photocatalytic activity, Catal. Sci. Tehnol. 5 (2015) 2522–2531.

[10] B.Y. Zheng, H. Zhao, A. Manjavacas, M. McClain, P. Nordlander, N.J. Halas, Distinguishing between plasmon-induced and photoexcited cariers in a device geometry, Nat. Commun. 6 (2015) 7797.

[11] S.Y. Moon, H.C. Song, E.H. Gwag, I.I. Nedrygailov, C. Lee, J.J. Kim, W.H. Doh, J. Y. Park, Plasmonic hot carrier-driven oxygen evolution reaction on Au nanoparticles/TiO_2 nanotube arrays, Nanoscale 10 (2018) 22180–22188.

[12] A. Wang, S. Wu, J. Dong, R. Wang, J. Wang, J. Zhang, S. Shong, S. Bai, Interfacial facet engineering on the Schootky barrier between plasmonic Au and TiO_2 in boosting the photocatalytic CO_2 reduction under ultraviolet and visible irradiation, Chem. Eng. J. 404 (2021) 127145.

[13] G. Žerjav, M. Roškarič, J. Zavašnik, J. Kovač, A. Pintar, Effect of Au loading on Schottky barrier height in TiO_2+Au plasmonic photocatalysts, Appl. Surf. Sci. 579 (2022) 152196.

[14] Š. Slapničar, G. Žerjav, J. Zavašnik, M. Finšgar, A. Pintar, Synthesis and characterization of plasmonic Au/TiO_2 nanorod solids for heterogeneous photocatalysis, J. Environ. Chem. Eng. 11 (2023) 109835.

[15] S.A. Hafezi, W.M. Abdel-Rahman, The endocrine disruptor bisphenol A (BPA) exerts a wide range of effects in carcinogenesis and response to therapy, Curr. Mol. Pharmacol. 12 (2019) 230–238.

[16] V. Reposi, A. Petala, Z. Frontistis, M. Antonopoulou, I. Konstantinou, D. I. Kondarides, D. Mantzavinos, Photocatalytic degradation of bisphenol A over Ph/TiO_2 supensions in different water matrices, Catal. Today 284 (2017) 59–66.

[17] M.I. Litter, Heterogeneous photocatalysis Transition metal ions in photocatalytic systems, Appl. Catal. B 29 (1999) 89–114.

[18] G. Žerjav, M.S. Arshad, P. Djinović, J. Zavašnik, A. Pintar, Electron trapping energy states of TiO_2-WO_3 compostes and their influence on photocatalytic degradation of bisphenol A, Appl. Catal. B 209 (2017) 273–284.

[19] G. Žerjav, J. Zavašnik, J. Kovač, A. Pintar, The influence of Schottky barrier height onto visible-light triggered photocatalytic activity of TiO_2+Au composites, Appl. Surf. Sci. 543 (2021) 148799.

[20] P. Verma, K. Mori, Y. Kuwahara, S. June Cho, H. Yamashita, Synthesis of plasmonic gold nanoparticles supported on morphology-controlled TiO_2 for aerobic alcohol oxidation, Catal. Today 352 (2020) 255–261.

[21] V. Brezová, D. Dvoranová, A. Staško, Characterization of titanium dioxide photoactivity following the formation of radicals by EPR spectroscopy, Res. Chem. Intermed. 33 (2007) 251–268.

[22] S. Flint, T. Markle, S. Thompson, E. Wallace, Bisphenol A exposure, effects, and policy: A wildlife perspective, J. Environ. Manage. 10 (2012) 19–34.

[23] S. Naniwa, K. Kato, A. Yamakata, A. Yamamoto, H. Yoshida, A quantitative study on the relationship of specific surface area and carrier lifetime to photocatalytic activity of anatase TiO_2 nanoparticles, ACS Catal. 13 (2023) 15212–15218.

[24] K.M. Reddy, C.V. Gopal Reddy, S.V. Manorama, Preparation, characterization, and spectral studies on nanocrystalline anatase TiO_2, J. Solid State Chem. 158 (2001) 180–186.

[25] C.F. Holder, R.E. Schaak, Tutorial on powder X-ray diffraction for characterizing nanoscale materials, ACS Nano 13 (2019) 7359–7365.

[26] H. Yazid, R. Adnan, M.A. Farrukh, Gold nanoparticles supported on titania for the reduction of *p*-nitrophenol, Ind. J. Chem. 52 (2013) 184–191.

[27] T. Zhao, M. Fang, Z. Tang, X. Zhao, F. Wu, J.P. Giesy, Adsorption, aggregation and sedimentation of titanium dioxide nanoparticles and nanotubes in the presence of different sources of humic acids, Sci. Total Env. 692 (2019) 660–668.

[28] S. Gagliardi, F. Rondino, C. Paoletti, M. Falconieri, On the morphology of nanostructured TiO_2 for energy applications: the shape of the ubiquitous nanomaterial, Nanomater. 12 (2022) 2608.

[29] C. Dette, M.A. Pérez-Osorio, C.S. Kley, P. Punke, C.E. Patrick, P. Jacobson, F. Giustino, S.J. Jung, K. Kern, TiO_2 anatase with a bandgap in the visible region, Nano Lett. 14 (2014) 6533–6538.

[30] S. Valencia, J.M. Marin, G. Restrepo, Study of the bandgap of synthesized titanium dioxide nanoparticules using the Sol-Gel method and a hydrothermal treatment, Open Mater. Sci. J. 4 (2010) 9–14.

[31] E. Chifor, I. Bordeianu, C. Anastasescu, J.M. Calderon-Moreno, V. Bratan, D.-I. Eftemie, M. Anastasescu, S. Preda, G. Plavan, D. Pelinescu, R. Ionescu, I. Stoica, M. Zaharescu, I. Balint, Bioactive coatings based on nanostructured TiO_2 modified with noble metal nanoparticles and lysozyme for Ti dental implants, Nanomater. 12 (2022) 3186.

[32] N.D. Abazović, M.I. Čomor, M.D. Dramićanin, D.J. Jovanović, S.P. Ahrenkiel, J. M. Nedeljković, Photoluminescence of anatase and rutile TiO2 particles, J. Phys. Chem. B 110 (2006) 25366–25370.

[33] V. Ghorbani, D. Dorranian, Properties of TiO_2/Au nanocomposite produced by pulser laser irradiation of mixture of individual colloids, Appl. Phys. A 122 (2016) 1019.

[34] V.V. Shimanovskaya, T.A. Khalyavka, G.A. Puchkovskaya, T.V. Bezrodna, V. V. Strelko, T.S. Veblaya, J. Baran, H. Ratajczak, Vibrational spectra and the structure peculiarity of TiO_2 different polycrystalline forms, SPIE Proc. 4938 (2001) 315–322.

[35] A. Nashim, K. Parida, n-$La_2Ti_2O_7$/p-$LaCrO_3$: a novel heterojunction based composite photocatalysts with enhanced photoactivity towards hydrogen production, J. Mater. Chem. A 2 (2014) 18405.

[36] S.I. Kol'tsov, S.P. Chapaikin, Binding energy of $2p_{3/2}$ electrons of titanium in titanium oxide layers synthesized by molecular lamination method, Theor. Exp. Chem. 27 (1991) 626–629.

[37] C. Fan, C. Chen, J. Wang, X. Fu, Z. Ren, G. Qian, Z. Wang, Black hydroxylated titanium dioxide prepared via ultrasonication with enhanced photocatalytic activity, Sci. Rep. 5 (2015) 11712.

[38] H. Ali-Löytty, M. Hannula, J. Saari, L. Palmolahti, B.D. Bhuskute, R. Ulkuniemi, T. Nyyssönen, K. Lahtonen, M. Valden, Diversity of TiO_2: controlling the molecular and electronic structure of atomic-layer-deposited black TiO_2, ACS Appl. Mater. Interfaces 11 (2019) 2758–2762.

[39] M. Sankar, Q. He, M. Morad, J. Pritchard, S.J. Freakley, J.K. Edwards, S.H. Taylor, D.J. Morgan, A.F. Carley, D.W. Knight, C.J. Kiely, G.J. Hutchings, Synthesis of stable ligand-free gold-palladium nanoparticles using a simple excess anion method, ACS Nano 6 (2012) 6600–6613.

[40] M.S. Arshad, Š. Trafela, K. Žužek Rožman, J. Kovač, P. Djinović, A. Pintar, Determination of Schottky barrier height and enhanced photoelectron generation in novel plasmonic immobilized multisegmented (Au/TiO_2) nanorod arrays (NRAs) suitable for solar energy conversion applications, J. Mater. Chem. 5 (2017) 10509–10516.

[41] A.M. Abdel-Mageed, K. Wiese, A. Hauble, J. Bansmann, J. Rabeah, M. Parlinska-Wojtan, A. Brückner, R.J. Behm, Steering the selectivity in CO_2 reduction on highly active Ru/TiO_2 catalysts: Support particle size effects, J. Catal. 401 (2021) 160–173.

[42] D.C. Hurum, A.G. Agrios, K.A. Gray, T. Rajh, M.C. Thurnauer, Explaining the enhanced photocatalytic activity of degussa P25 mixed-phase TiO_2 using EPR, J. Phys. Chem. B 107 (2003) 4545–4549.

[43] J.M. Coronado, A.J. Maira, J.C. Conesa, K.L. Yeung, V. Augugliaro, J. Soria, EPR study of the surface characteristics of nanostructured TiO_2 under UV irradiation, Langmuir 17 (2001) 5368–5374.

[44] C.P. Kumar, N.O. Gopal, T.C. Wang, M.-S. Wong, S.C. Ke, EPR investigation of TiO_2 nanoparticles with temperature-dependent properties, J. Phys. Chem. B 110 (2006) 5223–5229.

[45] T. Rajh, O.G. Poluektov, M.C. Thurnauer, Charge separation in titanium oxide nanocrystalline semiconductors revealed by magnetic resonance, Chemical Physics of Nanostructured Semiconductors (2003).

[46] H.E. Makmi, B. Deroide, Y. Bensimon, J.V. Zanchetta, Paramagnetic defects in solid sulphur and glasses of the system Ge–S, J. Non-Cryst. Solids 291 (2001) 78–85.

[47] L.-B. Xiong, J.-L. Li, B. Yang, Y. Yu, Ti^{3+} in the surface of titanium dioxide: generation, properties and photocatalytic application, J. Nanomater. 2012 (2011) 831524.

[48] O. Yalcin, Ferromagnetic resonance-theory and applications, InTech (2013).

[49] A.Y. Yermakov, V.R. Galakhov, A.S. Minin, V.V. Mesilov, M.A. Ulimin, K. Kuepper, S. Bartkowski, L.S. Molochnikov, A.S. Konev, V.S. Gaviko, G.S. Zakharova, Magnetic properties, electron paramagnetic resonance, and photoelectron spectroscopy studies of nanocrystalline TiO_2 co-doped with Al and Fe, Phys. Status Solidi B 258 (2021) 2000399.
[50] R. Ostruszka, G. Zoppellaro, O. Tomanec, D. Pinkas, V. Filimonenko, K. Šiškova, Evidence of Au(II) and Au(0) states in bovine serum albumin-Au nanoclusters revealed by CW-EPR/LEPR and peculiarities in HR-TEM/STEM imaging, Nanomat. 12 (2022) 1425.
[51] M. Agrachev, M. Ruzzi, A. Venzo, F. Maran, Nuclear and electron magnetic resonance spectroscopies of atomically precise gold nanoclusters, Acc. Chem. Res. 52 (2019) 44–52.
[52] S. Prusty, V. Siva, N. Shukla, B. Satpati, K. Senapati, P.K. Sahoo, Unusual ferromagnetic behaviour of embedded non-functionalized Au nanoparticles in Bi/Au bilayer films, RSC Adv. 6 (2016) 106584.
[53] M. Agrachev, S. Antonello, T. Dainese, M. Ruzzi, A. Zoleo, E. Aprà, N. Govind, A. Fortunelli, L. Sementa, F. Maran, Magnetic ordering in gold nanoclusters, ACS Omega 2 (2017) 2607–2617.
[54] U. Maitra, B. Das, N. Kumar, A. Sundaresan, C.N.R. Rao, Ferromagnetism exhibited by nanoparticles of noble metals, ChemPhysChem 12 (2011) 2322–2327.
[55] M. Marć, L. Majder-Kozdrowska, N. Guskos, G. Żołnierkiewicz, A.M. Montero, M. R. Dudek, The use of ultra-small Fe_3O_4 magnetic nanoparticles for hydrothermal synthesis of Fe^{3+}-doped titanate nanotubes, Mater. 13 (2020) 4612.
[56] T. Popescu, C.O. Matei, D.C. Culita, V.-A. Maraloiu, A.M. Rostas, L. Diamandescu, N. Iacob, T. Savopol, M.C. Ilas, M. Feder, A.-R. Lupu, A.C. Iacoban, I.D. Vlaicu, M. G. Moisescu, Facile synthesis of low toxicity iron oxide/TiO_2 nanocomposites with hyperthermic and photo-oxidation properties, Sci. Rep. 12 (2022) 6887.
[57] D. Toloman, A. Mesaros, A. Popa, O. Raita, T.D. Silipas, B.S. Vasile, O. Pana, L. M. Giurgiu, Evidence by EPR of ferromagnetic phase in Mn-doped ZnO nanoparticles annealed at different temperatures, J. Alloys Compd. 551 (2013) 502.
[58] E. Zhecheva, R. Stoyanova, E. Shinova, EPR analysis of the local structure of Ni^{3+} ions in Ni-based electrode materials obtained under high-pressure, J. Mater. Sci. 42 (2007) 3343–3348.
[59] D. Dvoranová, Z. Barbieriková, V. Brezová, Radical intermediates in photoinduced reactions on TiO_2 (an EPR spin trapping study), Molecules 19 (2014) 17279–17304.
[60] W. He, H. Jia, D. Yang, P. Xiao, X. Fan, Z. Zheng, H.-K. Kim, W.G. Wamer, J.-J. Yin, Composition directed generation of reactive oxygen species in irradiated mixed metal sulfides correlated with their photocatalytic activities, ACS Appl. Mater. Interfaces 7 (2015) 16440–16449.
[61] S. Zeng, E. Vahidzadeh, C.G. VanEssen, P. Kar, R. Kisslinger, A. Goswami, Y. Zhang, N. Mahdi, S. Riddell, A.E. Kobryn, S. Gusarov, P. Kumar, K. Shankar, Optical control of selectivity of high rate CO_2 photoreduction via interband-or hot electron Z-scheme reaction pathways in Au-TiO_2 plasmonic photonic crystal photocatalysts, App. Catal. B: Env. 267 (2020) 118644.
[62] M. Moskovits, Hot electrons cross boundaries, Science 332 (2011) 676–677.
[63] D. Shi, J. Liu, S. Ji, Preparation of Au/TiO_2 catalyst and the performance of liquid methanol catalytic oxidation to formic acid, Ind. Eng. Chem. Res. 56 (2017) 11028–11033.